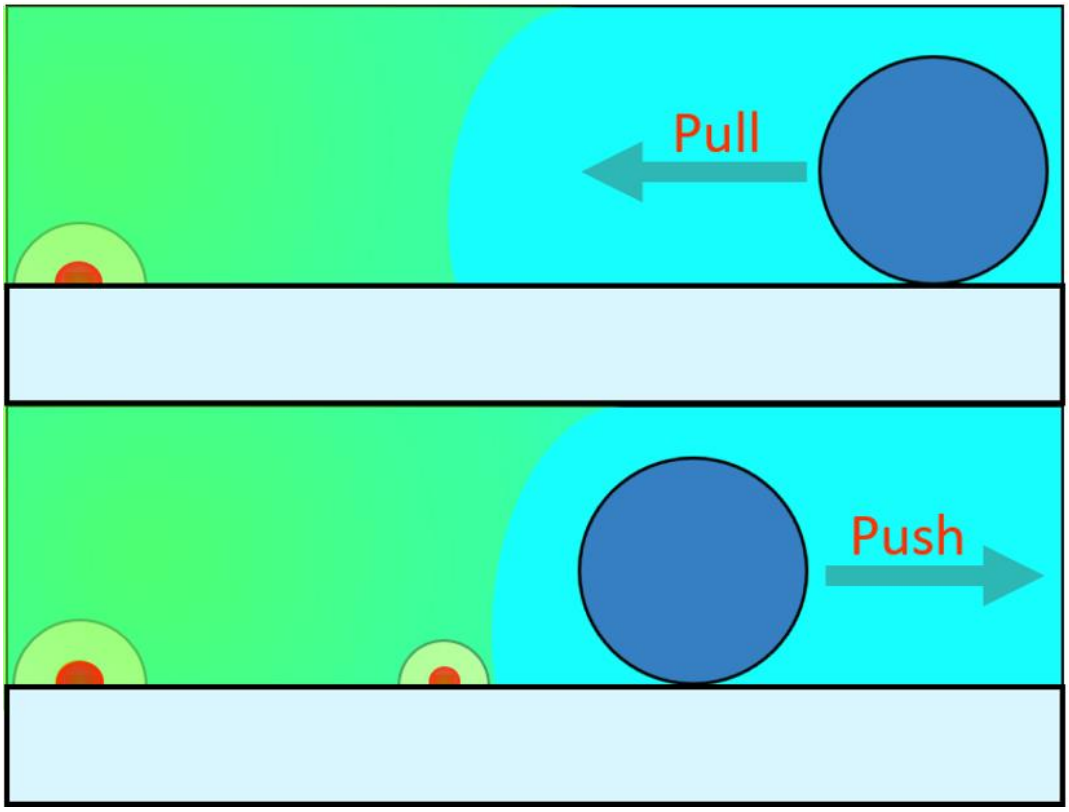

Measurements and simulations of thermoplasmonically induced Marangoni flows

Pantea Dara

DEPARTMENT OF PHYSICS

CHALMERS UNIVERSITY OF TECHNOLOGY

Gothenburg, Sweden 2023

www.chalmers.se

THESIS FOR THE DEGREE OF LICENTIATE OF TECHNOLOGY

Measurements and simulations of thermoplasmonically induced Marangoni flows

Pantea Dara

CHALMERS
UNIVERSITY OF TECHNOLOGY

Department of Physics
Chalmers University of Technology
Göteborg, Sweden, 2023

Division of Nano- and biophysics
Department of Physics
Chalmers University of Technology
SE-412 96 Gothenburg
Sweden
Telephone + 46 (0)31-772 1000

Cover:
Top: Microparticle get pulled toward one plasmonic vapor bubble
Bottom: Microparticle get pushed away from two plasmonic vapor bubbles

Printed. In Sweden by
Chalmers digital printing
Chalmers Tekniska Högskola
Gothenburg, Sweden 2023

CHALMERS UNIVERSITY OF TECHNOLOGY

Department of Physics

Measurements and simulations of thermoplasmonically induced Marangoni flows

Pantea Dara

Abstract

Particle transport in microfluidic environments is often dominated by slow diffusion near interfaces. However, by inducing localized fluid flow, it is possible to actively transport suspended nano-objects in confined spaces. One promising method for achieving precise and dynamic control over fluid flow on the microscale is to use photothermal effects based on the illumination of plasmonic metal nanoparticles, which exhibit very high optical absorption for light wavelengths near resonance. The particles can thus be used as nanoscale heat sources that locally increase the temperature of the surrounding fluid, resulting in processes such as thermophoresis, convection, and vapor bubble generation. This thesis focuses on the latter effect and the associated bubble nucleation and thermal Marangoni convection processes.
Marangoni flows result from the surface tension gradient that establishes on a thermoplasmonically induced vapor bubble at equilibrium. However, in addition to this, strong flow transients appear as a bubble is created and expands. Both phenomena lead to similar flow profiles. Here it is shown that the direction of these flows can be controlled by manipulating the temperature gradient on the surface of the bubble. Specifically, it is demonstrated that the direction of the strong transient flows around a nanobubble can be reverted by breaking the photothermal symmetry using two unequal nearby arrays of plasmonic nanoparticles. Furthermore, we investigate the possibility of remotely controlling the flow direction by turning the incident light polarization. The results are based on vectorial flow measurements using optical force microscopy supported by extensive flow profile simulations.

Keywords: thermoplasmonics, microfluidics, Marangoni flow, microbubbles, optical force microscopy

List of publications

The following paper is included in this thesis:

---

i. Directional control of transient flows generated by thermoplasmonic bubble nucleation.

Pantea Dara, Mohammad Mahdi Shanei, Steven Jones, and Mikael Käll
(Sbmitted)

Declaration of author contributions:

i: Performed all experiments and data analysis, designed, and simulated ellipsoidal plasmonic structure, modeled and simulated the flow profiles, and wrote the initial manuscript.

Acknowledgments

To my beloved parents, and my incredible brother. You are my best friends, my guides, my shoulder to lean on, and simply the best. My gratitude to you is beyond words.

Mikael, I sincerely appreciate your patience with me. I have gained a wealth of knowledge from you, not just as a researcher, but also in many other areas of life. Thank you so much for your guidance and support!

Steve, without you it would have been impossible. You were a great teacher and an incredible mentor. I was so lucky to get to know you and Dasha. Thank you, guys, for everything!

Mahdi, you are a fantastic researcher. Every day I am surprised by your intelligence and things you are capable of. Thank you so much for your help and support!

Betül, Adri and Emelie, your friendship is one of the most precious things I have gained since starting my PhD. You are incredibly smart, tremendously supportive and above all extremely kind.

Hana, Tom, Mindaugas, Vasilii, Mikaela, Santosh and Gosha thank you so much for your good energy and all the fun discussions we have during the lunch breaks. You guys are just great.

Timur, Battulga, Abhay, Sasha, Oleg, Daniel, Ximin, I feel extremely fortunate to be surrounded by such intelligent individuals like yourself. I have learned a lot from you just by seeing your approach to research. Seeing your passion for research motivates me. And Daniel, thank you so much for fabricating the first batch of my nanoantennae.

Charlotte and Caroline, thank you so much for all your help on the third-floor lab. I have learned so much from you. And Charlotte, thank you so much for all the support you gave me, especially over the past eight months.

Thanks to everyone else in Nano and Biophysics division, or it’s better to say in physics department. So many people have helped me with so many things.

And finally, I want to thank my supportive friends here in Chalmers, Shahrzad, Rujin and Tina. You know how much I appreciate your friendship.

Contents

Chapter 1

Introduction

The Marangoni flow, which was first reported by Giuseppe Matteo Marangoni in 1865, is the induced fluid flow along an interface due to an obtained surface tension gradient. As some simple examples, we can refer to tears of wine and self-propelled camphor disk boat that are described by this effect. In both cases, the spatial variation of a solute concentration (Alcohol or camphor) will create a surface tension gradient at the liquid interface, resulting in a flow from the alcohol/camphor-rich area to the water-rich area (Figure 1) [1].

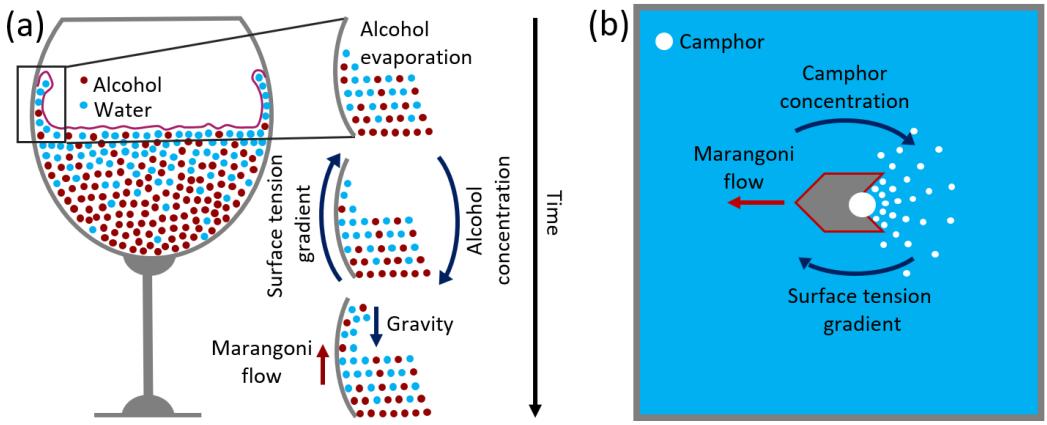

Figure 1. (a) Tears of wine form on a wine glass: Over time the alcohol in the wine evaporates from the surface at a rate higher than water, decreasing the concentration of alcohol in the meniscus. This creates a surface tension gradient that moves the meniscus up the walls of the glass leading to the formation of a film on the glass surface which is even more depleted of alcohol resulting in more wine getting pulled up. Finally, droplets will be formed, and the tears of wine will run down due to gravity. (b) self-propelled camphor disk boat: This vintage toy boat is propelled by a difference in surface tension. As the camphor mixes with water at the stern of the boat a gradient of surface tension is created pushing the boat forward.

In addition to the concentration gradient, other mechanisms can establish a surface tension gradient including a temperature gradient. In this case, this effect is referred to as the thermocapillary effect.

The spatial temperature variation at a liquid interface will lead to variations in surface tension, consequently creating unbalanced surface stress. This surface stress then will be compensated by a flow from the region with low surface tension (hot region) to the region with high surface tension (cold region) at the boundary. To conserve the fluid volume, for an incompressible fluid, the motion along the interface must be followed by the motion in the bulk. Therefore, the thermocapillary phenomenon induces a convective flow in the bulk of the heated fluid. Since the induced surface stress depends on the spatial temperature gradient and not on the value of the temperature, this effect can be very strong even for small changes in temperature, if the scale is small enough, making it a favorable mechanism to create flow in micro and nanoscale [2].

One of the most flexible and feasible platforms for achieving a desired temperature profile on the micro and nanoscale is plasmonic nanostructures [3]. Metallic nanostructures have shown great potential as local heat sources by enhanced absorption of light. The absorbed light excites collective electron motion in the metallic nanoparticle (i.e., plasmons), resulting in heat generation due to the Joule effect. Thus, the metallic nanoparticle will act as a hotspot that can locally increase the temperature of the surrounding fluid [4]. In addition, the polarization and chromatic dependence of the absorption cross-section of plasmonic nanostructures make them a great asset for achieving highly configurable temperature gradients [5-8]. Moreover, due to the enhanced light-matter interaction, these metallic nanostructures are able to rapidly superheat and vaporize the surrounding water into a microscopic bubble. The thermal surface tension gradient on the surface of this vapor bubble can in turn drive localized fluid flow due to the Marangoni effect [9-13], and provide an effective route toward optothermal manipulation at the micrometer scale.

This thesis is about manipulating the temperature gradient on a microbubble surface using plasmonic nanoantennas with the aim of controlling the flow on the bulk and close to the surface.

In Chapter 2, we will provide a brief overview of the physics underlying heat generation by plasmonic structures and the Marangoni flow. Additionally, we will review the equations that we employed to model and simulate these flows.

In Chapter 3, we will discuss the methods we used experimentally to measure the induced flows.

Finally, in Chapter 4 we will mention the remaining research questions and the possible outlooks. Finally, in Chapter 4, we will mention the remaining research questions and explore possible avenues for future research.

Chapter 2

Thermoplasmonics and Marangoni flow

In the past twenty years, there has been an increasing interest in the study of thermal processes driven by the heating of plasmonic nanoparticles, giving rise to the field of thermoplasmonics. Simple designs, biocompatibility, straightforward fabrication methods, and the ability to release heat on the nanoscale have made the plasmonic nanostructures the perfect heat sources that can be used for many applications including Photothermal therapy and cell biology, Photothermal and hot-electron chemistry, soft matters and fluids and solar light harvesting. In this chapter, we will mainly focus on the physics behind the plasmonic heat sources and their effect on a liquid medium. The spatial variation of temperature in liquids can drive many thermal processes, such as enhanced Brownian motion, thermo-viscous effects, thermo-osmosis, thermophoresis, convection, and phase change. Among these, convection (Marangoni convection) and phase change (vapor bubble generation) are the main processes relevant to our experiments [14, 15].

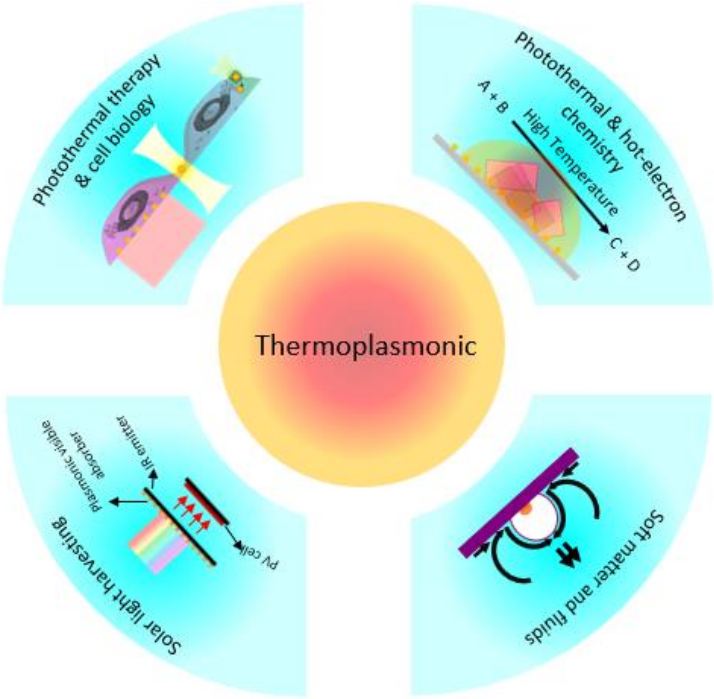

Figure 2:. Current research landscape in thermoplasmonics.

2.1. Scattering and absorption of light by metallic nanostructures

The scattering and absorption of light by plasmonic nanostructures, and the consequent temperature increase, are highly dependent on the shape and composition of the structures and the polarization and the wavelength of the incident light. To understand these dependencies

and how metallic structures can generate heat by absorption of light, we must first understand how light interacts with matter. In this section, we will discuss the simple case of elastic scattering and absorption of light by metallic nanoparticles, where nonlinear optical effects are not considered. So, we will consider a linear, nondispersive, homogenous medium in all cases. Light is an electromagnetic field, and it is described by two related vector fields that are a function of position and time: Electric field $\vec{E}(r,t)$ and magnetic field $\vec{H}(r,t)$. $\vec{E}$ and $\vec{H}$ oscillates in phase with one another and their direction of oscillation is orthogonal to one another and the direction of propagation. The relation between these two vector fields in any medium is governed by Maxwell's equations.

When light propagates through a source-free nonmagnetic conductive medium, Maxwell's equations in the differential form are written as:

$$\nabla \times \vec{H} = \frac{\partial}{\partial t}\vec{D} + \vec{J}, \quad 2\text{-}1$$

$$\nabla \times \vec{E} = -\frac{\partial}{\partial t}\vec{B}, \quad 2\text{-}2$$

$$\nabla \cdot \left(\epsilon_r \epsilon_0 \vec{E}\right) = 0, \quad 2\text{-}3$$

$$\nabla \cdot \left(\mu_r \mu_0 \vec{H}\right) = 0, \quad 2\text{-}4$$

where $\vec{D}(r,t)$, $\vec{B}(r,t)$, and $\vec{J}(r,t)$ are the electric displacement (electric flux density), magnetic flux density and electric current density and ϵ_0, ϵ_r, μ_0 and μ_r are permittivity of free space, relative permittivity, the permeability of free space, and relative permeability respectively.

Here, we will restrict our discussion to the interaction of electric field $\vec{E}(r,t)$ and the medium. As a result, we only need to focus on equation 2-1. But first, let's consider the simple case of having a dielectric medium instead of a conductive one, in the other word $\vec{J} = 0$ [16].

The electric displacement, $\vec{D}(r,t)$, is the response of a material to an external electric field, and it is determined by the macroscopic polarization density $\vec{P}$.

$$\vec{D} = \epsilon_0 \vec{E} + \vec{P}, \quad 2\text{-}5$$

the vectors $\vec{P}$ and $\vec{E}$ at every position and time are parallel and related as:

$$\vec{P} = \epsilon_0 \chi \vec{E}, \quad 2\text{-}6$$

where χ is called the electric susceptibility. By substituting 2-6 in 2-5 we will have:

$$\vec{D} = \epsilon_0 \vec{E} + \epsilon_0 \chi \vec{E} = \epsilon_0 (1+\chi)\vec{E}, \quad 2\text{-}7$$

where $(1+\chi)$ is called the relative permittivity, ϵ_r.

Now, if we consider a conductive medium such as metals, with linear conductive properties. We can define $\vec{J}$ as:

$$\vec{J} = \sigma \vec{E}, \quad 2\text{-}8$$

where σ is the conductivity. In this case, for a monochromatic wave of angular frequency ω, we can rewrite the equation 2-1 as:

$$\nabla \times \vec{H} = j\omega \epsilon_0 \epsilon_r \vec{E} + \sigma \vec{E} = j\omega\, \epsilon_c \vec{E}\,, \quad 2\text{-}9$$

where ϵ_c is the effective electric permittivity defined as:

$$\epsilon_c = \epsilon_0 \epsilon_r + \frac{\sigma}{\mathrm{j}\omega} = \epsilon_0 \epsilon_r \left(1 + \frac{\sigma}{j\omega \epsilon_0 \epsilon_r}\right) \quad 2\text{-}10$$

The effective permittivity is a complex, frequency-dependent parameter [16].

Since conductive metals have a slow response to an applied electric field at optical frequencies, we must consider a complex, frequency-dependent conductivity for them. One approach to do this is using the Drude model [16].

In the **Drude model**, we consider the conduction band electrons as an ideal gas of independent particles that move freely between scattering events, resulting in a frequency-dependent complex conductivity [16]:

$$\sigma = \frac{\sigma_0}{1+j\omega\tau}, \quad 2\text{-}11$$

where σ_0 is low-frequency conductivity and τ is the scattering time (or the relaxation time of the free electron gas) [16]. For a medium that has free-space-like dielectric properties with no other losses ($\epsilon = \epsilon_0$), from 2-10 and 2-11 we get the Drude relative effective permittivity as:

$$\epsilon_{drude} = 1 + \frac{\omega_p^2}{-\omega^2+j\omega\Gamma}, \quad 2\text{-}12$$

Where Γ is the damping factor and $\omega_p = \sqrt{\frac{\sigma_0}{\epsilon_0\tau}}$ is the plasma frequency. By defining $\sigma_0 = \frac{ne^2\tau}{m_e}$, we will have:

$$\omega_p = \sqrt{\frac{ne^2}{\epsilon_0 m_e}}, \quad 2\text{-}13$$

where n is the charge density and m_e is the effective electron mass [16].
Now, for adding the effect of intraband transitions, we can consider the Drude-Lorentz model:

$$\epsilon_{\text{Drude-Lorentz}} = 1 + \sum_{i=1}^{m} \frac{f_i\omega_p^2}{\omega_{0i}^2-\omega^2+j\Gamma_i\omega}, \quad 2\text{-}14$$

where ω_{0i}, Γ_i, f_i are the resonance frequency, damping frequency, and oscillator strength. This model is used to describe the complex permittivity of gold in all of the simulations done in this thesis with parameters according to ref. [17].
If the radius of the plasmonic structure, a, is much smaller than the wavelength of the incident light in the surrounding medium, $\lambda_m = \lambda_0/n_m$ (where λ_0 is the wavelength of light in free space and n_m is the refractive index of the surrounding medium), we can use the quasi-static approximation to determine the scattering and absorption cross sections. This is referred to as "Rayleigh" theory. According to Rayleigh theory, the scattering and absorption cross section of a spherical particle in a homogenous dielectric medium is defined as [18, 19]:

$$\sigma_{sca} = \frac{2}{3\pi}\frac{(2\pi a)^6}{\lambda_m^4}\left|\frac{\tilde{\epsilon}-1}{\tilde{\epsilon}+2}\right|^2 = \frac{8\pi^4}{3\lambda_m^4}|\alpha(\omega)|^2, \quad 2\text{-}15$$

$$\sigma_{abs} = \frac{-(2\pi a)^3}{\pi\lambda_m}\text{Im}\left(\frac{\tilde{\epsilon}-1}{\tilde{\epsilon}+2}\right) = \frac{2\pi}{\lambda_m}\text{Im}\{\alpha(\omega)\}, \quad 2\text{-}16$$

where $\tilde{\epsilon} = \frac{\epsilon_r}{\epsilon_m}$ is the ratio of complex relative permittivity of the metallic medium to the real relative permittivity of the dielectric medium and $\alpha(\omega) = 4\pi a^3\frac{\tilde{\epsilon}-1}{\tilde{\epsilon}+2}$ is the polarizability.
Based on 2-15 and 2-16 we can conclude that the absorption cross section is proportional to λ_m^{-1} and a^3 and scattering cross section is proportional to λ_m^{-4} and a^6 respectively. Unless the condition $\tilde{\epsilon} = -2$ is satisfied, in which the localized surface plasmon resonance will occur. For noble metals, the wavelength in which this condition is satisfied is in visible and near-infrared region.
One property of these plasmonic resonances is absorption enhancement, which will result in a temperature increase.
But, before discussing the heat generation by metallic nanostructures, we must explain that although the analytical solution for scattering an absorption given by Rayleigh theory gives us a good insight into how and why these properties change with size and wavelength and why an enhancement occurs, obtaining the cross sections of particles with arbitrary shapes is beyond the ability of Rayleigh or Mie solution. For these structures numerical methods such as the Finite-Difference Time-Domain method (FDTD) [20], and Finite Element Method (FEM) [21],

must be used for obtaining the scattering and absorption cross sections. Here, we have used a commercial FEM solver, COMSOL Multiphysics, to numerically calculate the absorption spectra of circular and ellipsoidal gold nanodisks.
One last thing that should be discussed in this section is the polarization dependency of the absorption cross section in elongated metallic nanostructures.
In contrast to symmetrical nanostructures, the absorption spectrum of elongated nanostructures has two plasmon bands that correspond to electron oscillations along their length (longitudinal mode) and across their section (transverse mode).
This shape effect can be simply described by using an anisotropic dynamical polarizability matrix:

$$\alpha(\omega) = \begin{Bmatrix} \alpha_{\perp}(\omega) & 0 & 0 \\ 0 & \alpha_{\parallel}(\omega) & 0 \\ 0 & 0 & \alpha_{\perp}(\omega) \end{Bmatrix} \qquad 2\text{-}17$$

For example, in the case of an ellipsoidal disk shown in the inset of figure 3, $\alpha_{\parallel}(\omega)$ and $\alpha_{\perp}(\omega)$ are the polarizability along the major (OY) and minor (OY) axes resulting in two peaks in the absorption spectrum. This property can be used for controlling heat generation by turning the incident polarization [22, 23].

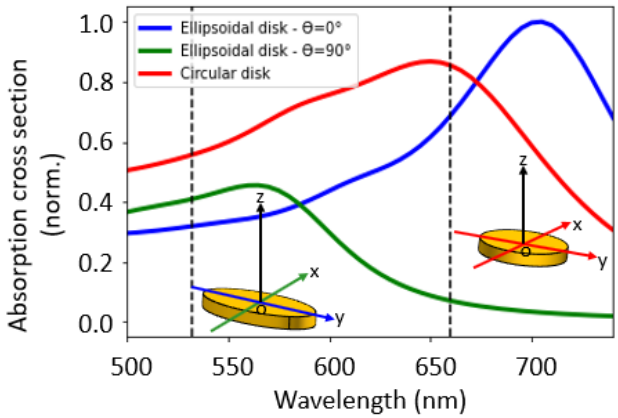

Figure 3: Absorption spectra of gold nanodisks (red, diameter 50 nm, height 60 nm) and nano ellipsoids (long axis diameter 100 nm, short axis diameter 50 nm, height 60 nm) for incident polarization parallel (blue) and perpendicular (green) to the long axis.

2.2. Heat generation by metallic nanostructures

As shown in section 2.1, metallic nanostructures are able to enhance the scattering and absorption of light at specific wavelengths in the visible and near-infrared regions due to their localized surface plasmon resonances. When metallic nanostructures are excited by light, the energy of incident photons will excite the collective oscillation of electrons which drives a current within the metal. Owing to the lossy nature of the metallic structures in optical frequencies, resistive heat will be generated in them. The delivered power by the nanostructure can be expressed either by the absorption cross section [4, 14]:

$$q(r) = \sigma_{abs} I/V, \qquad 2\text{-}18$$

where I is the irradiance of the incident light, and V is the volume of the nanostructure, or the oscillating current [4, 14]:

$$q(r,t) = \vec{J}(r,t).\vec{E}(r,t). \quad 2\text{-}19$$

Since the thermal processes happen during the continuous wave illumination are much slower than the electric field oscillations, we can use the averaged heat source density over the period of electromagnetic wave defined as [4, 14]:

$$q(r) = \frac{\omega}{2}\epsilon_0 Im\{\epsilon_r(\omega)\}\left|\vec{E}(r)\right|^2. \quad 2\text{-}20$$

In our simulations, equation 2-18 is used to calculate the generated heat by nanostructures.

After the generated heat (absorbed power) is calculated, it is possible to calculate the heat dissipation within the nanoparticle and the surrounding medium. To do so, we can consider two main heat transfer mechanisms: conduction and convection. The model that can be used for heat transfer is [24-27]:

$$\left(\rho C_p \frac{\partial T}{\partial t} - k\nabla^2 T\right) + \rho C_p \mathbf{u}\cdot\nabla T = q, \quad 2\text{-}21$$

where ρ, C_p, k are the material density, the material heat capacity at constant pressure, and the material thermal conductivity, and q is the calculated heat source density [24-27].

The first term in equation 2-21 models the conduction heat transfer. Conduction is the process of thermal energy transition via collisions between neighboring atoms/molecules. ρ and C_p determine how much energy is required to increase the temperature of the material, and k describes the relation between the heat flux vector and the temperature gradient, in other words, it describes the ability of the material to conduct heat.

The second term in equation 2-21 models the convection heat transfer. In this mechanism, thermal energy transition is due to the transport of the hot fluid molecules, and it is governed by the fluid velocity field, **u**. We will talk more about the heat induced fluid flows in section 2.3.

It should be mentioned that, in addition to convection and conduction, radiation is the third fundamental heat transfer mechanism. However, this mechanism is generally inefficient in plasmonic systems. As a result, it has been neglected in all of the simulations done in this thesis [27].

Also, according to our simulations, it was observed that the induced fluid flow does not have a significant effect on heat dissipation and the resulting temperature profile, making conduction the dominant mechanism for heat dissipation in our system.

Before finishing this section, we will discuss the thermoplasmonic vapor bubbles.

Naturally, when the temperature of the water increases, above a certain temperature, a vapor bubble will nucleate. Surprisingly, this very simple phenomenon that we have observed so many times in macro scales, while boiling water for example, has a very complicated mechanism in the microscale which has been the subject of many studies.

Here, we will only focus on the bubble formation, growth, and dissipation under continuous wave illumination in water via a thermoplasmonic system.

So many thermoplasmonic systems have been designed for generating and studying microbubbles. We can divide these systems into two categories: continuous and isolated structures. In continuous structures, such as continuous plasmonic films or distributed arrays of metallic nanostructures, the size of the bubble is determined by the laser focal spot size [11, 28-30]. Meanwhile, in isolated structures the size is determined by the size of the structure [10, 31, 32]. Therefore, it is possible to heat several isolated structures separately, using a single large laser beam without being worried about creating one giant bubble.

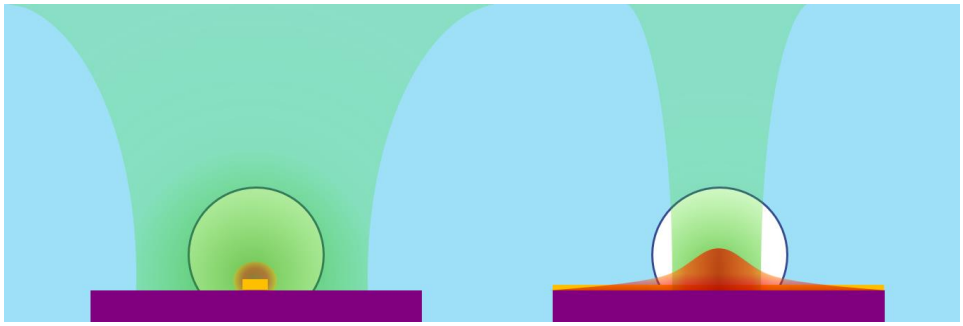

Figure 4: Left: Generated bubble on top of an isolated plasmonic structure. In this case, the size of the bubble is controlled by the size of the structure. Right: Generated bubble on top of a continuous plasmonic structure. In this case, the size of the bubble is controlled with the laser focal spot size.

Regardless of the structure, in thermoplasmonic systems, the surface in which the bubble is generated is smooth and clean. As a result, no nucleation site, or cavities, exists on the surface. According to trapped vapor theory, these air-filled cavities make the water boil at 100℃, which is the known water boiling point [33]. But, for smooth surfaces, the temperature in which the phase transition actually happens is between 100℃ and water spinodal temperature. Spinodal temperature, is the temperature in which the liquid cannot remain in a liquid state anymore.

The next stage is bubble growth. It has been explained that the growth of the thermoplasmonic bubble has two phases. The first phase includes the nucleation and growth of the bubble due to the direct vaporization of superheated water. The second phase is the growth of the bubble due to the diffusion of the dissolved gas molecules from the superheated water into the bubble. Since the second phase is almost continuous, the generated bubble can be enlarged to hundreds of micrometres [34].

The last stage is bubble dissipation. In most applications, we are more interested in creating small bubbles (with a diameter of less than 2μm) that can dissipate fast (less than 1ms). It has been shown that the presence of the dissolved gas in the bubble is the main reason for its slow dissipation, and the dissipation rate depends on the initial bubble size [35, 36].

One solution to decrease the bubble lifetime is utilizing degassed water [11, 12, 28, 29]. In this case, the second phase of growth will be prohibited. Although this method is very useful for the case of continuous structures, it might not be feasible in many applications, both due to the complex and time-consuming preparation of degassed water and the inevitable re-dissolving of air into water over time [34, 37]. However, in the case of isolated structures, the bubble size is decreased due to the spatial extension of the metallic structure. In this case, due to the reduction of the volume of heated water, the bubble size will decrease to a few micrometres, which can dissipate very quickly [31]. This makes the isolated structures a better candidate for applications in which we need to have dynamic control over bubble nucleation and dissipation.

So far, Namura et al. reported the emergence of plasmonic bubbles using both continuous (Gold nanofilms) [11, 12, 28, 29], and isolated plasmonic structures (Gold micropetals) [10] in degassed water with sizes around 5~10 μm.

In addition, Jones et al. have shown that it is possible to increase the temperature locally by utilizing spatially isolated plasmonic nanoantennas (Circular gold nanodisks) for heat generation in air-equilibrated water. They were able to decrease the bubble size to less than 1μm, which could dissipate very quickly, making it an excellent tool for achieving rapid dynamic control [31].

2.3. Heat induced flows

2.3.1. Persistent flow

Here we will concentrate on the fluid velocity fields, **u**, that are driven by the buoyancy effect or surface tension created by thermal effects.
The buoyancy driven flow is generated due to the decreasing of the fluid density with increasing temperature. In most materials the density changes linearly with temperature :

$$\rho = \rho_0 - \beta\rho_0(T - T_0) \qquad 2\text{-}22$$

Where β is the thermal expansion coefficient. Thus, the heated fluid will rise into the cooler region and the cooler fluid from the surroundings will flow into the heated region.
The surface tension driven flow is generated due to the decrease of surface tension with increasing temperature on a boundary. Similar to density, surface tension, γ, also changes linearly with temperature, T [2]:

$$\frac{d\gamma}{dT} = \gamma_T \qquad 2\text{-}23$$

Where γ_T is the surface tension coefficient. In the following, we will see that γ_T can be used to relate the normal component of the shear stress to the tangential derivative of the temperature.
The velocity of buoyancy or surface tension driven flows is usually small; therefore, the fluid motion can be described by the Boussinesq approximation of the Navier-Stokes equations for an incompressible fluid ($\nabla . \boldsymbol{u} = 0$) [38]:

$$\frac{\partial \boldsymbol{u}}{\partial t} + (\boldsymbol{u}.\nabla)u = -\frac{1}{\rho}\nabla p + \nu\nabla^2\boldsymbol{u} + g\beta T\overrightarrow{e_z} \qquad 2\text{-}24$$

Where ν is the kinematic viscosity and is equal to dynamic viscosity μ, divided by the density. p is the fluid pressure, and we assume a homogenous gravity field $\vec{g} = -g\overrightarrow{e_z}$.
To consider the thermal Marangoni effect the following boundary condition that acts at the free surface of the fluid (typically a gas-liquid interface) must be considered [38]:

$$[-pI + \mu(\nabla\boldsymbol{u} + (\nabla\boldsymbol{u})^T)]\hat{n} = \gamma(\nabla_t \cdot \hat{n})\hat{n} - \nabla_t\gamma \qquad 2\text{-}25$$

By replacing the 2-23 into 2-25, we will have:

$$[-pI + \mu(\nabla\boldsymbol{u} + (\nabla\boldsymbol{u})^T)]\hat{n} = \gamma(\nabla_t \cdot \hat{n})\hat{n} - \gamma_T\nabla_t T, \qquad 2\text{-}26$$

where, $\hat{n}$ is the outward directed unit normal vector to the air/water (bubble) interface. The first term on the right side of equation 2-26 is the Laplace pressure and represents the normal forces that create the curvature of the interface. The second term, however, represents the tangential forces that are created due to the temperature gradient [38].
We have used equations 2-21, 2-24, and 2-26 to simulate the fluid velocity field, **u,** and the heat transfer in our system.
At this point, we have realized that the induced flow pattern created due to the Marangoni effect is proportional to the tangential derivative of the temperature on the air/water (bubble) interface. This means that for the case of a single bubble nucleated on top of a heat source demonstrated in figure 5.a, the flow on the bubble surface will be from the bottom to the top, which then will be followed by two symmetrical vortices in the bulk and finally an induced flow on the substrate surface which is directed toward the heat source. This induced flow on

the substrate (water/glass interface) is so important since due to the no slip boundary condition we expect almost zero velocity close to the surface.
Considering this argument, one straightforward way for controlling the flow close to the substrate is to manipulate the temperature gradient on the bubble surface. This can be easily done by adding another heat source on one side of the preliminary heat source and breaking the symmetry of the temperature profile. In this way in addition to the out-of-plane temperature gradient, we will also have an in-plane temperature gradient. This will induce a flow from the warmer side of the bubble to the colder side of it (from the right to the left for the example illustrated in figure 5.b.

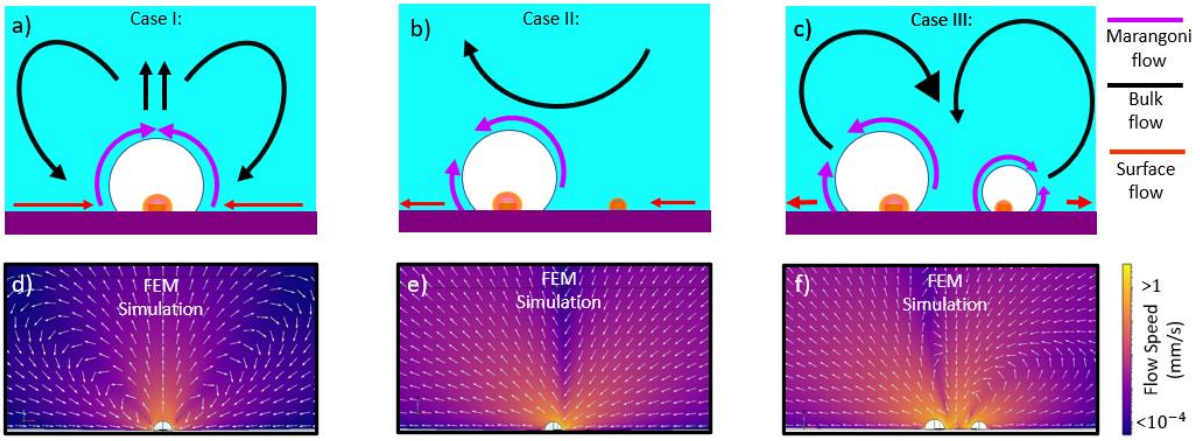

Figure 5: Expected Marangoni flow induced by a) Case I: a single bubble with a temperature gradient normal to the interface and b) Case II: a single bubble with temperature gradients both perpendicular and parallel to the surface c) Case III: by two unequal nearby bubbles with an additional temperature gradient parallel to the surface. (d) to (f) FEM simulations of Marangoni flows induced by the same structures in (a) to (c).

Now, if the temperature induced by the second heat source was enough to vaporize the surrounding water, another bubble will appear. This will result in much more complicated flow patterns that depend on the size of the bubbles, the temperature of the heat sources, and more interestingly, the position of the bubbles.
The induced flow due to the Marangoni effect, can also displace the bubble from its initial position. Figure 6 shows the displacement of a $6\mu m$ bubble with the flow. The structure here consists of a primary array of isolated nanoantennas with 19 circular nanodisks and a secondary array of isolated nanoantennas with 7 circular nanodisks, and the heating laser is modulated with $f_m = 5$ hz. The setup and the structures will be explained in detail in the experimental methods section.
This displacement can intensify the effect of the inplane temperature gradient since one side of the bubble will get closer to the heat source.

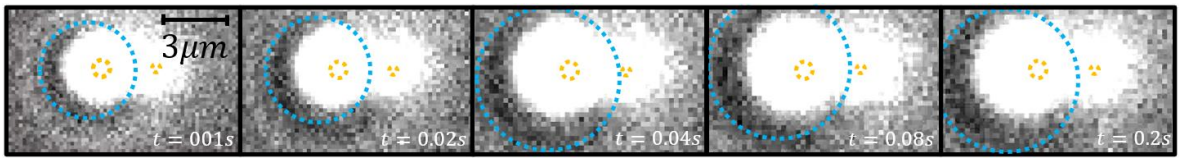

Figure 6. The displacement of a 6μm bubble with the flow. The blue circles indicate the position and the size of the bubble within time. The yellow circle on the left is the position of the primary array of isolated nanoantennas with 19 circular nanodisks and on the right is the secondary array of isolated nanoantennas with 7 circular nanodisks. The heating laser is modulated with $f_m = 5$ hz.

Figure 5.c shows the induced flow when each of the generated bubbles is pushed away in the direction parallel to the temperature gradient existing on their surfaces.
Figure 5.d to e shows the FEM simulations of the three situations explained above.
Finally, although we have not used the concentration gradient to create the Marangoni flow in our simulations, the effect can be simply taken into account by adding the $\gamma_c \nabla_t C$ to the right side of the 2.25. γ_c is the surface tension coefficient that relates the normal component of the shear stress to the tangential derivative of the concentration and C is the concentration. In some cases, the concentration, C also depends on the temperature itself (for example in a water/alcohol solution). In this case, the existing temperature gradient on the bubble surface can induce both thermal and concentrational Marangoni flows. It has been reported by Namura et al. that the direction of the flow around a vapor bubble can be reversed by generating vapor bubbles in alcohol/water mixtures instead of water. In this case, a gradient of the alcohol molecular population will be induced on the bubble's surface, which will create reverse surface tension and flow.

2.3.2. Transient flow

In addition to the persistent flow explained in the previous section, it has been demonstrated by Jones et al. that the microbubbles nucleated on isolated plasmonic nanostructures are able to induce strong transient flows with velocities >1 mm/s [32]. The direction of this induced fluid flow is ascribed to the Marangoni force and therefore depends on the temperature gradient on the bubble surface. The origin of the transient is not completely understood, but it may be attributed to transient pressure waves emitted by vapor bubble generation. It has been demonstrated that the emission of this strong transient pressure wave is due to the fast formation of a vapor/liquid interface under the very high temperature gradients generated at the nanoparticle/water interface [36]. To model the pressure wave emitted by the generation and expansion of the bubble, we are not allowed to use the Boussinesq approximation anymore, and we have to use the Navier-Stokes equation for a compressible fluid ($\nabla . \boldsymbol{u} \neq 0$). This means that the term $-{}^{2}/_{3}\, \nu(\nabla . \boldsymbol{u})$ will be added to the right side of equation 2-24. Moreover, we have to add the term $-l(r)\nabla . \boldsymbol{u}$ to equation 2-21 in which $-l(r)$ is the Clapeyron coefficient and represent the flow velocity field induced due to the vaporization of the liquid [39].
Since it has been experimentally shown that the profile of the transient flows is the same as the Marangoni flow, we have only simulated the Marangoni flow in this thesis.

2.4. Stokeslet Approximation

The solution for the flow velocity around a microscopic bubble nucleated on a no-slip interface can be obtained by embedding a singular point force (*Stokeslet*) at the distance $(+h)$ from a stationary no-slip plane boundary in an infinite viscous fluid (V), and its image (*Stokeslet image*) at the distance $(-h)$ form the boundary [40].
Figure 7 shows the image system and its relevant vectors. Here, $\vec{X} = (X_1, X_2, X_3)$ is the coordinate of the point (P) in which we want to calculate the velocity, $\vec{y} = (y_1, y_2, h)$ and $\overrightarrow{y'} = ({y'}_1, {y'}_2, -h)$ are the coordinates of the Stokeslet and Stokeslet image, and the translated coordinates $\vec{r} = (r_1, r_2, r_3)$, and $\vec{R} = (R_1, R_2, R_3)$ are defined as $(\vec{X} - \vec{y})$ and $(\vec{X} - \overrightarrow{y'})$, respectively [40].

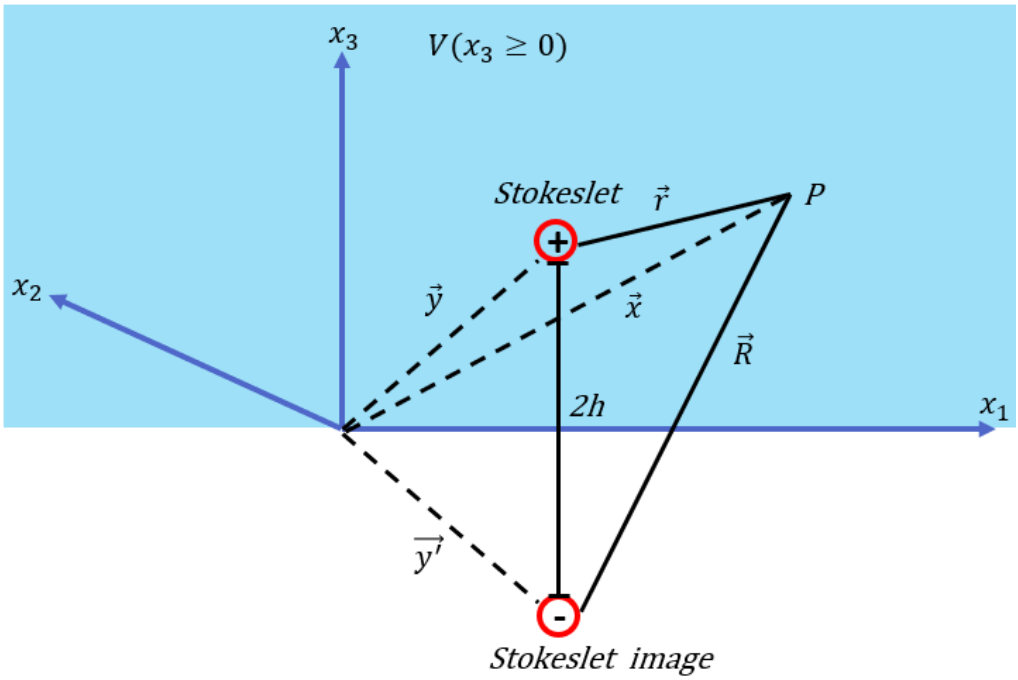

Figure.6: The position of stokeslet and image, and relevant vectors $\vec{X}$, $\vec{r}$and $\vec{R}$.

The velocity vector can be calculated by:

$$u_i = F_j G_i^j \qquad 2\text{-}27$$

Where F_j is the amplitude of the Stokeslet in the j direction and G_i^j is the Green's function. So, all we have to do is to construct the green function. Here,

$$G_i^j = u_i^j + v_i^j \qquad 2\text{-}28$$

Where, u_i^j and v_i^j are the fundamental singular solutions due to the Stokeslet and Stokeslet image, respectively [40].

Let's start with u_i^j. To obtain u_i^j, we need to solve the equation 2-24, considering the point source as a unit vector in j direction at $\vec{X} = \vec{y}$. Lucky for us, we are able of making the problem much simpler by following assumptions [40-42]:

1- We will only consider the steady state flows ($\frac{\partial u}{\partial t} = 0$).

2- Since the inertial forces are very small in comparison to the viscous forces, we will consider $(u.\nabla)u \approx 0$.

3- We will consider the image as point force of equal magnitude, but of opposite sign.

4- We consider the plane boundary to be $x_3 = 0$ ($u = 0$ *on* $x_3 = 0$).

5- And finally, we ignore any other external forces including gravity.

Considering these assumptions, equation 2-24 can be written as:

$$\nabla \boldsymbol{p^j} = \mu \nabla^2 \boldsymbol{u^j} + \boldsymbol{e^j} \delta(X - y) \qquad 2\text{-}29$$

The solution to this equation can be obtained by implementing a three-dimensional Fourier transform with suitable conditions at infinity. This results in the following velocity components:

$$u_i^j = \frac{1}{8\pi\mu}\left[\frac{\delta_{ij}}{r} + \frac{r_i r_j}{r^3}\right], \qquad 2\text{-}30$$

in which, $r = \sqrt[2]{(r_1^2 + r_2^2 + r_3^2)}$ is the distance between the Stokeslet and the point (P).
Now, we turn to the problem of obtaining complementary solution v_i^j. The Navier-Stokes equation can be written as:

$$\nabla \boldsymbol{q^j} = \mu\nabla^2 \boldsymbol{v^j} - \boldsymbol{e^j}\delta(X - y'), \qquad 2\text{-}31$$

where $\boldsymbol{q^j}$, and $\boldsymbol{v^j}$ are the complementary pressure and velocity singularities. To solve this equation, we have to consider the following boundary condition:

$$\boldsymbol{v^j}(S) = -\boldsymbol{u^j}(S), \qquad 2\text{-}32$$

where S defines the set of points on the plane boundary. This will guarantee the no-slip condition on the boundary.
Considering this condition and by implementing a two-dimensional Fourier transform the solution for v_i^j is:

$$v_i^j = \frac{1}{8\pi\mu}\left[-\left[\frac{\delta_{ij}}{R} + \frac{R_i R_j}{R^3}\right] + 2h\left(\delta_{j\alpha}\delta_{\alpha k} - \delta_{j3}\delta_{3k}\right)\frac{\partial}{\partial R_k}\left\{\frac{hR_i}{R^3} - \left[\frac{\delta_{i3}}{R} + \frac{R_i R_3}{R^3}\right]\right\}\right] \qquad 2\text{-}33$$

Where $\alpha = 1{,}2$, and δ_{ij} signifies the Kronecker delta while the tensor $\left(\delta_{j\alpha}\delta_{\alpha k} - \delta_{j3}\delta_{3k}\right)$ is non-zero only when $j = k$ and equal to +1 for $j = 1$ or 2, and -1 for $j = 3$, and $R = \sqrt[2]{(R_1^2 + R_2^2 + R_3^2)}$ is the distance between the Stokeslet image and the point (P) [42].
Finally, by substituting 2-32 and 2-33 in 2-28, u_i will be defined as:

$$u_i = \frac{F_j}{8\pi\mu}\left[\left[\frac{\delta_{ij}}{r} + \frac{r_i r_j}{r^3}\right] - \left[\frac{\delta_{ij}}{R} + \frac{R_i R_j}{R^3}\right] + 2h\left(\delta_{j\alpha}\delta_{\alpha k} - \delta_{j3}\delta_{3k}\right)\frac{\partial}{\partial R_k}\left\{\frac{hR_i}{R^3} - \left[\frac{\delta_{i3}}{R} + \frac{R_i R_3}{R^3}\right]\right\}\right] \qquad 2\text{–}34$$

Figure 8 shows the stokeslet simulations for three cases introduced in section 2.3.1. To model case I, it's enough to assume one stokeslet, $S_1 = (0, 0, F_3)$, on $(0, 0, h_1)$. However, for case II, we should add a force pointing in x direction in order to model the temperature gradient in that direction. This will result in a tilted stokeslet, $S_2 = (F_1, 0, F_3)$, on $(0, 0, h_1)$. Finally, for Case III, we assumed two tilted Stokeslets in opposite directions, S_3 and S_4 to model the two bubbles with opposing in plane temperature gradients.

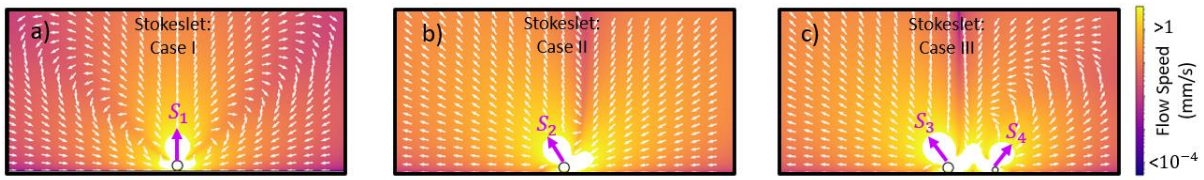

Figure.8: Stokeslet simulations of Marangoni flow induced by a) Case I: a single bubble with a temperature gradient normal to the interface and b) Case II: a single bubble with temperature gradients both perpendicular and parallel to the surface c) Case III: by two unequal nearby bubbles with an additional temperature gradient parallel to the surface.

Chapter 3

Research Methods

In this chapter, we will review the research methods used in our experiments.

3.1. Holographic optical tweezing

As its name suggests, optical tweezers use optical forces to tweeze an object. So, to realize how optical tweezers work, one must first understand what optical forces are.
It was first predicted by Maxwell and Bartoli in the 1870s that radiation pressure exists due to the momentum of light [43]. One specific example to illustrate this momentum is the case of plane-wave light normally incident onto a flat, perfect mirror. The magnitude of the momentum that each photon carries is equal to $^{h}/_{\lambda}$, and its direction is in the direction of light propagation. However, when the light gets reflected (not transmitted), the magnitude of the momentum remains the same, but its direction is reversed. This will result in a $^{2h}/_{\lambda}$ net change of momentum per photon, which will impart a force on the mirror due to the conservation of momentum. This force is called the radiation pressure force and acts to push particles in the direction of incident light [43].
In more general terms, phenomena such as scattering, and absorption can stop the transmission of light. The total power not transmitted by the particle due to these phenomena must convey a force upon the particle, which is calculated by:

$$F_{radiation} = \frac{n_m}{c_0} P_{extinct}, \qquad 3\text{-}1$$

in which, n_m is the refractive index of the particle and $P_{extinct}$ is the total power lost due to the extinction of transmitted light:

$$P_{extinct} = (\sigma_{sca} + \sigma_{ab}) I_0, \qquad 3\text{-}2$$

where, I_0 is the intensity of incident light, and σ_{sca} and σ_{abs} are defined in chapter 2.
Another important optical force, which is the main force in optical tweezing, is the gradient force. The gradient force is due to the gradient of the intensity of incident light, and it pulls the particle into regions of higher electric field intensity [44].
When a sub-wavelength particle is illuminated by linearly polarized monochromatic light, it will act as a dipole. The dipole moment of the particle is calculated by [44]:

$$\vec{p} = \epsilon_0 \epsilon_{\mathrm{m}} \alpha \vec{E}, \qquad 3\text{-}3$$

where $\alpha(\omega)$ is the polarizability that we defined in Chapter 2. The induced force due to the interaction of this dipole and the external electromagnetic field (Lorentz force) can be written as:

$$\vec{F}_{\text{Lorentz}} = (\vec{p}\cdot\nabla)\vec{E} + \frac{d\vec{p}}{dt}\times\vec{B} = \epsilon_0\epsilon_{\text{m}}\alpha\left((\vec{E}\cdot\nabla)\vec{E} + \frac{\partial\vec{E}}{\partial t}\times\vec{B}\right) \quad 3\text{-}4$$

By using the vector identity $\nabla(\vec{A}_1\cdot\vec{A}_2) = \vec{A}_1\times(\nabla\times\vec{A}_2) + \vec{A}_2\times(\nabla\times\vec{A}_1) + (\vec{A}_1.\nabla)\vec{A}_2 + (\vec{A}_2.\nabla)\vec{A}_1$ with $\vec{A}_1 = \vec{A}_2 = \vec{E}$, we will have:

$$(\vec{E}.\nabla)\vec{E} = \frac{1}{2}\nabla|E|^2 - \vec{E}\times(\nabla\times\vec{E}) \quad 3\text{-}5$$

By replacing 3-5 into 3-4 and using the Faraday's law ($\nabla\times\vec{E} = -\partial_t\vec{B}$), we will have:

$$\vec{F}_{\text{Lorentz}} = \frac{1}{2}\epsilon_0\epsilon_{\text{m}}\alpha\nabla|E|^2 + \epsilon_0\epsilon_{\text{m}}\alpha\frac{\partial}{\partial t}(\vec{E}\times\vec{B}) \quad 3\text{-}6$$

Taking the time average of 3-6, we will have:

$$\vec{F}_{\text{gradient}} = \langle\vec{F}_{\text{Lorentz}}\rangle_t = \frac{1}{4}\epsilon_0\epsilon_{\text{m}}\alpha\nabla|E|^2 + \epsilon_0\epsilon_{\text{m}}\alpha\mu_0\frac{\partial I_0}{\partial t}, \quad 3\text{-}7$$

where μ_0 is the permeability of free space. Finally, if we assume a time-constant electric field intensity, the optical gradient force will be defined as:

$$\vec{F}_{\text{gradient}} = \frac{1}{4}\epsilon_0\epsilon_{\text{m}}\alpha\nabla|E|^2 \quad 3\text{-}8$$

As can be observed from equation 3-8, for positive polarizability, the gradient force pulls the particles along the electric field intensity gradient.

One way to achieve very strong electric field gradient is by focusing a laser beam using a high numerical aperture objective. One practical approach to gain a better understanding of how a focused laser beam can trap a particle is the ray-optics approximation illustrated in figure 9.b. In case I, since the particle is positioned at the focal spot, the momentum of the transmitted light will be same as the incident light, therefore no gradient force will act on the particle. However, when the particle is lightly displaced from the focal point (case II to case IV), then the transmitted light momentum will change, and this change of momentum will result in exerting a force upon the particle and pulling it back to the focal spot. For small displacements from the equilibrium position, the restoring optical force change linearly with the displacement along each axis, making the restoring force Hookean:

$$\vec{F}_{\text{i,gradient}} = K_i\Delta r_i \quad 3\text{-}9$$

In which, K_i and Δr_i are the spring constant and the displacement along the i axis, respectively.

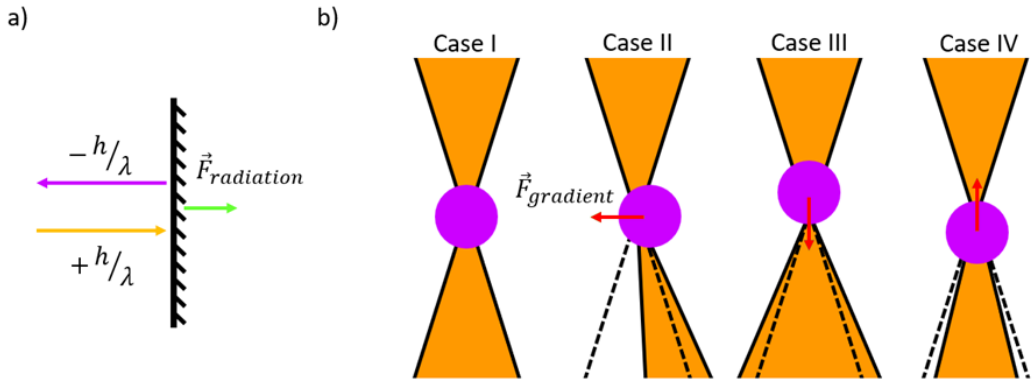

Figure.9: Ray optic illustration of (a) Radiation pressure force act on a perfect mirror. (b) gradient forces act on a dielectric sphere when case I: the particle is at the focal spot (no gradient force). Case II to case IV: the particle is slightly displaced from the focal spot.

Now, if we are able to move the focal spot of the laser, we can use it to transport the trapped particle. One way to do this is to utilize a *4-f correlator*. Figure 10 shows how the changes in direction and convergence of light at conjugate Fourier plane, will change the position of the laser focal spot at the trapping objective image plane.

So, the question now is how we can control the direction and convergence of light at the conjugate Fourier plane?

One approach to achieve this is the *holographic optical tweezing* technique. In this technique a Spatial Light Modulator (SLM) is used to control the light phase profile at a specific plane. In our experiments we have used a "liquid crystal on silicon"-SLM which consists of a 2D array of liquid crystal cells on top of a reflective silicon mirror. Each element in this array can be controlled by an applied voltage, which changes the orientation of the liquid crystal molecules. As a result, the reflected beam phase profile can be controlled by creating a specific optical path length for each pixel in the 2D array. Therefore, by placing the SLM at a conjugate Fourier plane, it is possible to control the spatial distribution of $\vec{k}$.

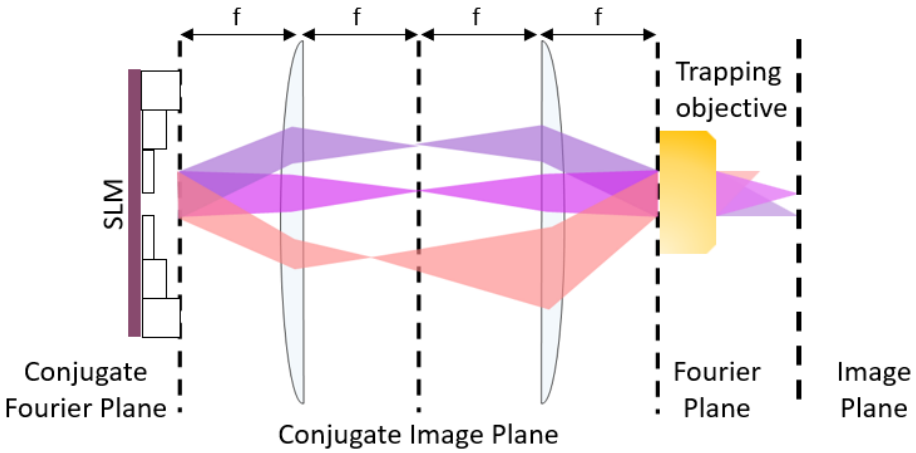

Figure.10: An SLM and a 4-f correlator used to control the position of the trapping laser focal spot. Three cases are shown: nominal beam path (bright purple), deflected beam path (dark purple), deflected and convergent beam path (pink).

3.2. Optical force microscopy

3.2.1. Quadrant Photo Diode

As mentioned in the previous section, any perturbation in the position of the trapped particle position will cause a change in the direction of the transmitted light. These small changes can be measured to determine any external forces (Marangoni or transient flow for example) that may have caused this displacement. To do so we can collect the intensity distribution of transmitted light, using a Quadrant Photo Diode (QPD) at the conjugate Fourier plane. The QPD consists of four photodiodes arranged in a 2X2 array shown in figure 11. The voltage output signals of the QPD are the difference between the intensity of light detected by the top and bottom rows (ΔBT), left and right columns (ΔLR), and sum of all four quadrants ($\sum$).
Figure 11.b illustrates how, for the cases discussed and plotted in figure 9.b, the intensity distribution of the transmitted light changes on QPD plane.
In order to be able to use this method to measure the particle displacement, we have to make sure that a linear change in the voltage signal corresponds to a linear change in the particle position. In another word, a linear change in the particle position must result in a linear change in the transmitted light momentum (a.k.a $\vec{k}$ vector distribution), guaranteeing that the restoring force is Hookean. To check this condition, an adhered bead on microscope slide was scanned in front of the trapping focal spot by moving a piezo stage with a known velocity along each principal axis, which confirmed that we are operating within the linear regime.

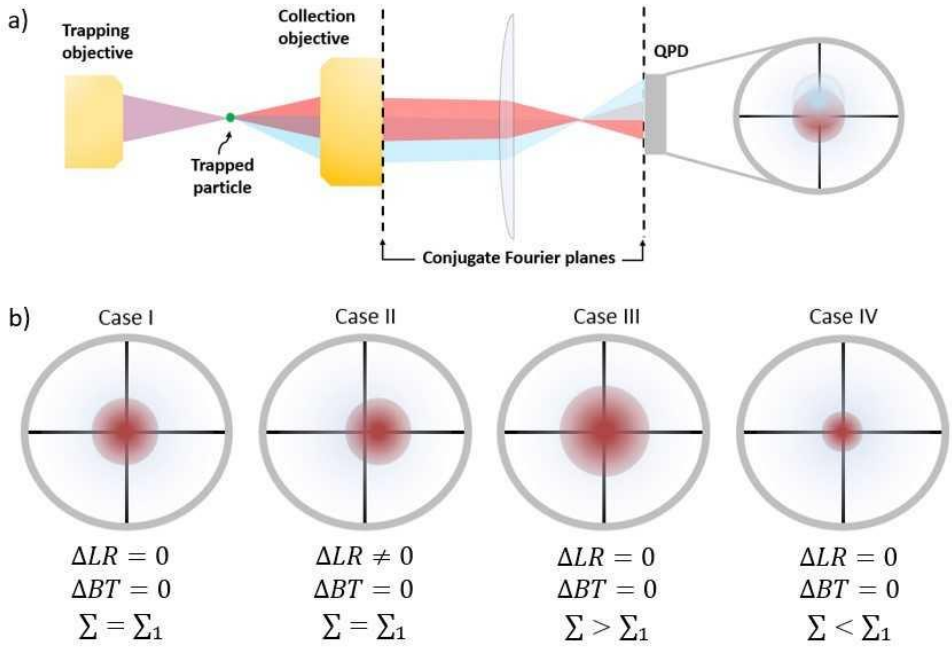

Figure.11: a) Overview of the experimental setup used for measuring trapped particle displacement via transmitted light. The back focal plane (Fourier plane) of the collection objective is imaged onto a QPD. b) How particle displacement in the cases discussed and plotted in figure 9.b changes the intensity distribution on QPD.

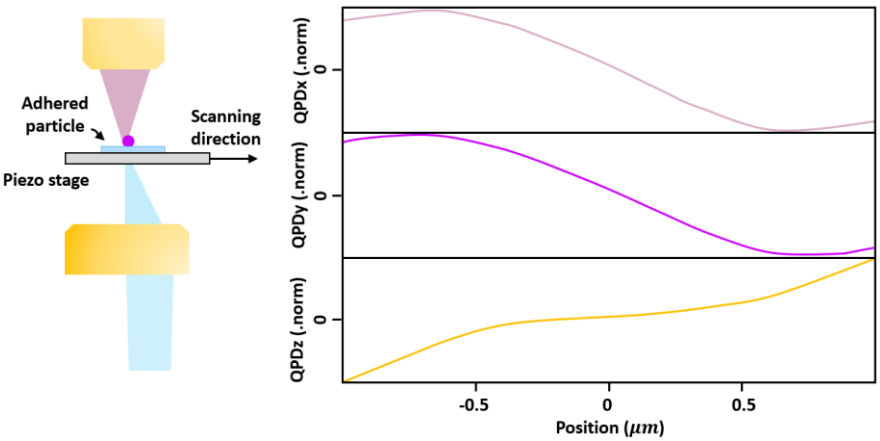

Figure.12: Left: Overview of the experimental setup used for testing that particle displacements are within the linear regime. A 2 μm microsphere is attached to a glass slide and scanned through the laser focal spot along each coordinate axis. Right: The lines show the QPD response vs the bead displacement from its nominal position.

Finally, in order to convert the collected data from signals in volt to displacement in meters, we need to calibrate our QPD response. A trapped object, within the linear regime, can be approximated as a Brownian particle in a harmonic potential. To gain a better insight of this approximation, and how we can use it for our calibration, we should first briefly discuss Brownian motion.

3.2.2. Brownian motion

Brownian motion arises from the random kinetic impulses exerted by adjacent fluid molecules. The Langevin equation can be used to model how these random kinetic impulses affect the motion of a particle in a fluid.
Given that we used spherical microbeads in our experiments, we modeled the particle in our study as a rigid sphere in a viscous medium. The kinetic impulses exerted by the adjacent fluid molecules were represented by the stochastic force, $F_{thermal}$. Lastly, it is important to note that we are considering a free particle moving in one direction (x), and that the system is in thermal equilibrium.

$$m\ddot{x}(t) + \gamma_0 \dot{x} = F_{thermal} \qquad 3\text{-}10$$

Here, $m\ddot{x}(t)$ is the inertial term and m is the mass of the particle, $\gamma_0 \dot{x}$ is the drag force and γ_0 is the Stokes drag coefficient. For a spherical particle with radius a, the Stokes drag force is equal to $6\pi\eta a$. Where η is the viscosity of the medium.
Let's start with multiplying both side of 3-10 by x, and take the ensemble average:

$$m\langle x\ddot{x}\rangle + \gamma_0\langle x\ddot{x}\rangle = \langle xF_{thermal}\rangle \qquad 3\text{-}11$$

Since there is no correlation between the thermal force and the position and considering the random nature of the force with a mean of zero, the term on the right-hand side of the equation will be zero. Also, by considering $\frac{d}{dt}\langle x\dot{x}\rangle = \langle x\ddot{x}\rangle + \langle \dot{x}^2\rangle$, equation 3-11 will turn into:

$$m(\frac{d}{dt}\langle x\dot{x}\rangle - \langle \dot{x}^2\rangle) + \gamma_0\langle x\dot{x}\rangle = 0 \qquad 3\text{-}12$$

We know based on the equipartition theory, that in thermal equilibrium, the thermal energy is equally shared among all degrees of freedom, so for a spherical particle moving in one dimension, the average kinetic energy is $\frac{1}{2}m\langle \dot{x}^2\rangle = \frac{1}{2}k_BT$, where k_B is Boltzmann constant, and T is the absolute temperature. As a result, equation 3-12 can be written as:

$$\frac{d}{dt}\langle x\dot{x}\rangle = \frac{k_BT}{m} - \frac{\gamma_0}{m}\langle x\dot{x}\rangle \qquad 3\text{-}13$$

If we take the ansatz $\langle x\dot{x}\rangle = A_0e^{-\gamma_0\frac{t}{m}} + A_1$ (where A_0 and A_1 are constants), and insert it into equation 3-13, we realize that A_1 must be equal to ${k_BT}/{\gamma_0}$. So we can write $\langle x\dot{x}\rangle$ as:

$$\langle x\dot{x}\rangle = A_0e^{-\gamma_0\frac{t}{m}} + {k_BT}/{\gamma_0} \qquad 3\text{-}14$$

Now, if we take the limit as $t \to \infty$ for 3-14:

$$\lim_{t\to\infty}\langle x\dot{x}\rangle = {k_BT}/{\gamma_0} \qquad 3\text{-}15$$

Considering that $\frac{d}{dt}\langle x^2\rangle = 2\langle x\dot{x}\rangle$ and solving for $\langle x^2\rangle|_{t\to\infty}$ gives:

$$\langle x^2\rangle = \frac{2k_BT}{\gamma_0}t = 2Dt \qquad 3\text{-}16$$

The term $\langle x^2\rangle$ is referred to as the Mean Squared Displacement (MSD) and is useful for characterizing the diffusion of Brownian particles. As we can observe, MSD has a linear dependence on time, with a proportionality constant, D, which is commonly referred to as the diffusivity.

Now, let's define the thermal force as $F_{thermal} = \varrho\xi(t)$, where ϱ is the amplitude of the Brownian motion, and $\xi(t)$ is a Gaussian random variable that accounts for the stochastic nature of the thermal force. We can discard the inertial term in the Langevin equation in the long-time limit and simplify it to only include the drag force and thermal force.

$$\dot{x} = \frac{\varrho}{\gamma_0}\xi \;\rightarrow\; x - x_0 = \frac{\varrho}{\gamma_0}\int_0^t \xi(t')dt', \qquad 3\text{-}17$$

Where x_0 is the value of x at $t = 0$.

Now, if we consider $x_0 = 0$, by squaring both side of the equation and take the ensemble average:

$$\langle x^2\rangle = \frac{\varrho^2}{\gamma_0^2}\int_0^t \langle \xi^2\rangle dt \qquad 3\text{-}18$$

Since $\langle \xi^2\rangle = 1$, we will have:

$$\langle x^2\rangle = \frac{\varrho^2}{\gamma_0^2}t + C_0 \qquad 3\text{-}19$$

Since we considered x_0 is equal to zero, then C_0 must also be zero. By comparing equations 3-16 and 3-19, we get:

$$\varrho = \sqrt{2k_B T\gamma_0} \qquad 3\text{-}20$$

This equation shows the dependency of Brownian motion to the drag force.
As we mentioned in the previous section, a trapped object, within the linear regime can be approximated as a Brownian particle in a harmonic potential. To add the harmonic potential to our model, we simply should add the restoring Hookean force. In this case, the Langevin equation can be expressed as follows, while still discarding the inertial term:

$$\gamma_0 \dot{x} + Kx = \sqrt{2k_B T\gamma_0}\,\xi(t) \qquad 3\text{-}21$$

Now, if we take the Fourier transform of this equation, we will have:

$$\tilde{x} = \frac{\sqrt{2k_B T\gamma_0}\,\tilde{\xi}}{K - i\omega\gamma_0} \qquad 3\text{-}22$$

Finally, if we obtain the Power Spectral Density (PSD) in the long-time limit, using equation 3-22, we will get:

$$PSD = \frac{2k_B T\gamma_0}{K^2 + \omega^2{\gamma_0}^2} \qquad 3\text{-}23$$

By defining a characteristic frequency $f_c = K/2\pi\gamma_0$, we will have:

$$PSD = \frac{D}{2\pi^2(f_c^2 + f^2)} \qquad 3\text{-}24$$

3.2.3. QPD calibration

Now, for calibrating the QPD signal, first, we trap a probe particle and collect the time series obtained by the QPD for a limited time, then we convert this time series to PSD, and fit it with equation 3-23, and extract the diffusivity, $D_i({}^{V^2}/_{Hz})$ along i direction ($i = 1, 2, and\ 3$). Then we calculate the conversion factor, $\beta_i({}^{m}/_{V})$ by:

$$\beta_i = \sqrt{\frac{D_i(h)}{D_i}}, \qquad 3\text{-}25$$

where, h is the distance from the boundary, and $D_i(h)({}^{m^2}/_{Hz})$ is equal to $k_B T/\gamma_i(h)$. Where, $\gamma_i(h)$ is the is Stokes' drag coefficient for the probe particle, corrected for boundary effects using Faxén's law.

$$\gamma_{\parallel} = \gamma_0 \left[1 - \frac{9}{8}\frac{a}{2h} + \left(\frac{a}{2h}\right)^3 + \frac{45}{16}\left(\frac{a}{2h}\right)^4 - 2\left(\frac{a}{2h}\right)^5\right]^{-1} \qquad 3\text{-}26$$

$$\gamma_{\perp} = \gamma_0 \left[\frac{4}{3} \sinh(\beta) \sum_{n=1}^{\infty} \left\{ \frac{n(n+1)}{(2n-1)(2n+3)} \times \left(\frac{2\sinh\big(\mathrm{B}(2n+1)\big) + (2n+1)\sinh(2\mathrm{B})}{4sinh^2(\mathrm{B}\left(n+\frac{1}{2}\right) - (2n+1)^2 sinh^2(\mathrm{B})} - 1 \right) \right\} \right], \quad \text{3-27}$$

where, $\gamma_{\parallel}$ and $\gamma_{\perp}$ are the drag coefficients for directions parallel and perpendicular to the boundary, respectively, and B is equal to $\cosh^{-1}(\frac{h}{a})$.

Then, by multiplying the time series by the conversion factor, we will convert our signal to the particle displacement in meter.

In our experiments, we typically perform the calibration step at the beginning of each measurement before inducing any flow in the system. This involves collecting the QPD signal of a trapped particle for one second and following the steps outlined above to extract the conversion factor.

3.2.4. Measurement of Marangoni and transient forces

To measure the external forces exerted on the trapped particle by the Marangoni and the transient flow, we employed the following equation:

$$F_{ex,i} = K_i x_i + \gamma_i(h) \frac{dx_i}{dt} \quad \text{3-28}$$

In this equation, x_i represents the displacement along each axis after inducing a flow, K_i is equal to $2\pi\gamma_i(z)f_{c,i}$, where $f_{c,i}$ is extracted by fitting the PSD of x_i with equation 3-23, and $\gamma_i(h)$ is calculated using 3-26 and 3-27. To calculate the velocity, we simply divide the equation above by $\gamma_i(h)$.

3.3. Thermoplamonic bubble generation and detection

The physical mechanism for bubble generation was explained in Chapter two. In this section, we will briefly describe the structures and setup used for bubble generation and detection.

To create a temperature gradient parallel to the substrate surface, we employed two arrays of isolated nanoantennas placed next to each other, and we investigated two different arrangements of gold nanoantenna arrays.

In the first arrangement, both arrays consisted of circular nanoantennas, and a 532nm laser was used as a heating laser. In the second arrangement, one of the arrays had disks replaced by ellipsoidal nanoantennas, which have a polarization-dependent absorption cross-section. For this arrangement, we used a 660nm laser as a heating laser to create a more significant difference in light absorption at different polarizations. In both cases, the primary array was

made up of 19 gold circular nanodisks with a diameter of 100 nm, and the heating laser was focused on this array. Meanwhile, the secondary array comprised 7 circular and 39 ellipsoidal gold nanodisks in the first and second arrangement. The major and minor axes of the ellipsoidal disks were 100 nm and 50 nm, respectively, and the distance between the two arrays was 2000 nm.

The selected sizes and arrangement of the plasmonic nanoantennas facilitated the production of small bubbles in air-equilibrated water, which dissipated rapidly after the heating laser was turned off. Additionally, the distance between the two structures was significant enough to prevent the formation of a single large bubble over both arrays. The heating laser used in the experiments had a wavelength of either 532 or 660 nm and was modulated in a square wave temporal profile with a duty cycle of 50% and frequency f_m. In the first arrangement, changes in the intensity of the bubble detection laser (633 nm), which was also focused on the primary array, were used to detect bubble generation in air-equilibrated water. However, in the second arrangement, the wavelengths of the bubble detection laser and heating laser were close, making it impossible to detect the bubbles. Finally, a 1064 nm laser was used for both holographic optical tweezing and optical force microscopy. Figure 13 shows the schematic drawing of the experimental setup.

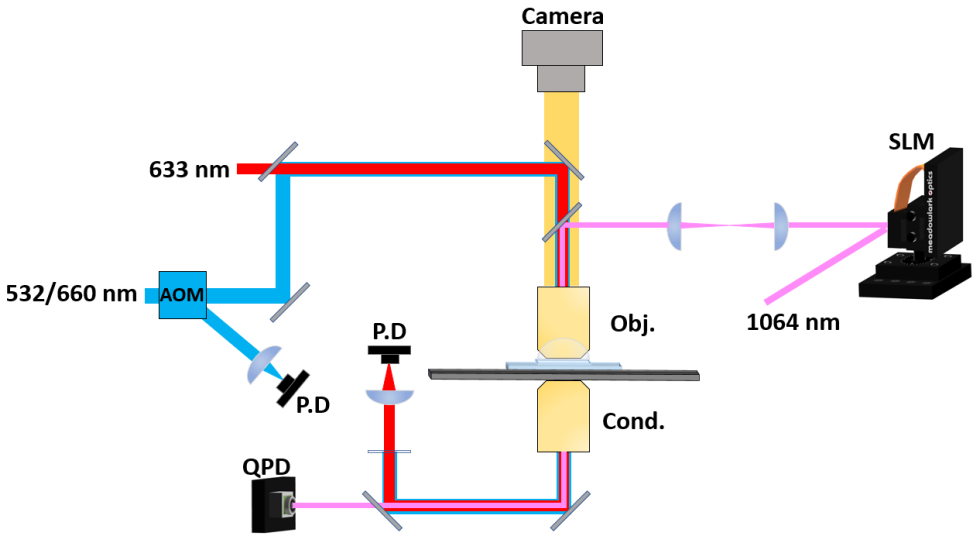

Figure.13: Schematic drawing of the experimental setup.

Chapter 4

Conclusion and outlook

The concepts discussed in this thesis demonstrate that thermoplasmonic bubbles can be used for creating local flows which can be remotely controlled. Especially, it was shown that it is possible to actively create and control the direction of the flows close to an interface where no-slip condition exists.

The flexibility of plasmonic heat sources, and the dependency of the amplitude and the direction of these flows to the temperature gradient on the bubble surface, makes it possible to achieve a desired flow profile by engineering the plasmonic nanostructures.

Furthermore, it was shown that it is possible to simulate these flows using both the Stokeslet approximation and FEM, which can be used as an extra tool to design and predict the flow patterns induced by plasmonic structures.

Here, we have shown how the flow profile changes when we use two closely spaced dissimilar arrays of plasmonic nanoantennae. So, one question raised here is what will happen if we increase the number of these antennas and change the distance between them? Is it possible to design a periodic array of absorbing elements, and engineer the absorption of each element based on the rotation or size of the element? In other words, is it possible to design a thermoplasmonic metasuraface?

Another question worth investigating is whether it is possible to create micro bubbles using dielectric structures or dielectric metasurfaces.

And finally, the most significant unanswered question here is the nature of the flow transients. While we have discussed the emission of shock waves due to bubble generation, even if we accept that the origin of these flow transients is the emission of pressure waves, we still need to answer the question of why the flow profile of this flow is the same as the Marangoni flow.

References

1. Dai, Q., et al., *Directional interfacial motion of liquids: Fundamentals, evaluations, and manipulation strategies.* Tribology International, 2021. **154**: p. 106749.
2. Baroud, C.N., *Thermocapillarity*, in *Encyclopedia of Microfluidics and Nanofluidics*, D. Li, Editor. 2013, Springer US: Boston, MA. p. 1-7.
3. Baffou, G., et al., *Deterministic temperature shaping using plasmonic nanoparticle assemblies.* Nanoscale, 2014. **6**(15): p. 8984-8989.
4. Baffou, G. and R. Quidant, *Thermo-plasmonics: using metallic nanostructures as nano-sources of heat.* Laser & Photonics Reviews, 2013. **7**(2): p. 171-187.
5. Chen, H., et al., *Gold nanorods and their plasmonic properties.* Chemical Society Reviews, 2013. **42**(7): p. 2679-2724.
6. Girard, C., et al., *Designing thermoplasmonic properties of metallic metasurfaces.* Journal of Optics, 2018. **20**(7): p. 075004.
7. Kharintsev, S.S., et al., *Designing two-dimensional temperature profiles using tunable thermoplasmonics.* Nanoscale, 2022. **14**(33): p. 12117-12128.
8. Jing, Z., et al., *Active spatial control of photothermal heating and thermo-actuated convective flow by engineering a plasmonic metasurface with heterodimer lattices.* Photonics Research, 2022. **10**(11): p. 2642-2657.
9. Koji Takahashi, J.-G.W.C.-L.T., *MARANGONI EFFECT IN MICROBUBBLE SYSTEMS.* Microscale Thermophysical Engineering, 1999. **3**(3): p. 169-182.
10. Namura, K., et al., *Gold Micropetals Self-Assembled by Shadow-Sphere Lithography for Optofluidic Control.* Advanced Materials Interfaces, 2022. **9**(18): p. 2200200.
11. Namura, K., et al., *Photothermally controlled Marangoni flow around a micro bubble.* Applied Physics Letters, 2015. **106**(4): p. 043101.
12. Namura, K., K. Nakajima, and M. Suzuki, *Quasi-stokeslet induced by thermoplasmonic Marangoni effect around a water vapor microbubble.* Scientific Reports, 2017. **7**(1): p. 45776.
13. Setoura, K., S. Ito, and H. Miyasaka, *Stationary bubble formation and Marangoni convection induced by CW laser heating of a single gold nanoparticle.* Nanoscale, 2017. **9**(2): p. 719-730.
14. Baffou, G., *Thermoplasmonics: Heating Metal Nanoparticles Using Light*. 2017, Cambridge: Cambridge University Press.
15. Baffou, G., F. Cichos, and R. Quidant, *Applications and challenges of thermoplasmonics.* Nature Materials, 2020. **19**(9): p. 946-958.
16. Saleh, B.E. and M.C. Teich, *Fundamentals of photonics*. 2019: john Wiley & sons.
17. Rakić, A.D., et al., *Optical properties of metallic films for vertical-cavity optoelectronic devices.* Applied optics, 1998. **37**(22): p. 5271-5283.
18. Cox, A., A.J. DeWeerd, and J. Linden, *An experiment to measure Mie and Rayleigh total scattering cross sections.* American Journal of Physics, 2002. **70**(6): p. 620-625.
19. Young, A.T., *Rayleigh scattering.* Phys. Today, 1982. **35**(1): p. 42-48.
20. Yee, K., *Numerical solution of initial boundary value problems involving Maxwell's equations in isotropic media.* IEEE Transactions on antennas and propagation, 1966. **14**(3): p. 302-307.
21. Reddy, C., *Finite element method for eigenvalue problems in electromagnetics*. Vol. 3485. 1994: NASA, Langley Research Center.
22. Girard, C., et al., *Designing thermoplasmonic properties of metallic metasurfaces.* Journal of Optics, 2018. **20**(7): p. 075004.
23. Sattler, K.D., *Handbook of nanophysics: nanoparticles and quantum dots*. 2016: CRC press.

24. Aćimović, S.S., et al., *Antibody–antigen interaction dynamics revealed by analysis of single-molecule equilibrium fluctuations on individual plasmonic nanoparticle biosensors.* ACS nano, 2018. **12**(10): p. 9958-9965.
25. Landau, L.D. and E.M. Lifshitz, *CHAPTER V - THERMAL CONDUCTION IN FLUIDS*, in *Fluid Mechanics (Second Edition)*, L.D. Landau and E.M. Lifshitz, Editors. 1987, Pergamon. p. 192-226.
26. Landau, L.D. and E.M. Lifshitz, *CHAPTER VI - DIFFUSION*, in *Fluid Mechanics (Second Edition)*, L.D. Landau and E.M. Lifshitz, Editors. 1987, Pergamon. p. 227-237.
27. Cengel, Y. and T.M. Heat, *A practical approach.* Heat and Mass Transfer, 2003.
28. Namura, K., et al., *Direction control of quasi-stokeslet induced by thermoplasmonic heating of a water vapor microbubble.* Sci Rep, 2019. **9**(1): p. 4770.
29. Namura, K., et al., *Self-Oscillation of Locally Heated Water Vapor Microbubbles in Degassed Water.* Advanced Materials Interfaces, 2020. **7**(18): p. 2000483.
30. Kim, Y., H. Ding, and Y. Zheng, *Enhancing surface capture and sensing of proteins with low-power optothermal bubbles in a biphasic liquid.* Nano letters, 2020. **20**(10): p. 7020-7027.
31. Jones, S., et al., *Ultrafast Modulation of Thermoplasmonic Nanobubbles in Water.* Nano Letters, 2019. **19**(11): p. 8294-8302.
32. Jones, S., et al., *Strong Transient Flows Generated by Thermoplasmonic Bubble Nucleation.* ACS Nano, 2020. **14**(12): p. 17468-17475.
33. Cho, H.J. and E.N. Wang, *Bubble nucleation, growth, and departure: A new, dynamic understanding.* International Journal of Heat and Mass Transfer, 2019. **145**: p. 118803.
34. Wang, Y., et al., *Vapor and Gas-Bubble Growth Dynamics around Laser-Irradiated, Water-Immersed Plasmonic Nanoparticles.* ACS Nano, 2017. **11**(2): p. 2045-2051.
35. Baffou, G., et al., *Super-Heating and Micro-Bubble Generation around Plasmonic Nanoparticles under cw Illumination.* The Journal of Physical Chemistry C, 2014. **118**(9): p. 4890-4898.
36. Li, J., et al., *Photothermal generation of programmable microbubble array on nanoporous gold disks.* Optics Express, 2018. **26**(13): p. 16893-16902.
37. Liu, X., et al., *Formation and dissolution of microbubbles on highly-ordered plasmonic nanopillar arrays.* Sci Rep, 2015. **5**: p. 18515.
38. Kuhlmann, H.C. *Thermocapillary Convection*. in *Free Surface Flows*. 1998. Vienna: Springer Vienna.
39. Lombard, J., et al., *Strong and fast rising pressure waves emitted by plasmonic vapor nanobubbles.* Physical Review Research, 2021. **3**(2): p. 023231.
40. Blake, J.R., *A note on the image system for a stokeslet in a no-slip boundary.* Mathematical Proceedings of the Cambridge Philosophical Society, 1971. **70**(2): p. 303-310.
41. Blake, J., *A model for the micro-structure in ciliated organisms.* Journal of Fluid Mechanics, 1972. **55**(1): p. 1-23.
42. Blake, J.R. and A.T. Chwang, *Fundamental singularities of viscous flow.* Journal of Engineering Mathematics, 1974. **8**(1): p. 23-29.
43. Požar, T., et al., *Isolated detection of elastic waves driven by the momentum of light.* Nature Communications, 2018. **9**(1): p. 3340.
44. Ulanowski, Z. *Optical tweezers-principles and applications*. in *Proc. Roy. Microsc. Soc*. 2001.

Paper I

Directional control of transient flows generated by thermoplasmonic bubble nucleation.

Pantea Dara, Mohammad Mahdi Shanei, Steven Jones, and Mikael Käll

Submitted